RICE UNIVERSITY

CHAOTIC IONIZATION OF A RYDBERG ATOM SUBJECTED TO ALTERNATING KICKS

by

Shuzhen Ye

A Thesis Submitted
in Partial Fulfillment of the
Requirements for the Degree

Master of Science

Approved, Thesis Committee:

F.B. Dunning, Advisor
Professor and Chair of Physics and Astronomy

T.C. Killian
Professor of Physics and Astronomy

Q. Si
Professor of Physics and Astronomy

Houston, Texas

April, 2011

CHAOTIC IONIZATION OF A RYDBERG ATOM SUBJECTED TO ALTERNATING KICKS

Shuzhen Ye

Abstract

Quasi-one-dimensional Rydberg atoms exposed to alternating positive and negative electric field pulses (kicks) are an example of a chaotic atomic system. Chaotic ionization is predicted in this system via a phase space turnstile mechanism, and we have explored this experimentally. Turnstiles form a general transport mechanism for numerous chaotic systems, and this study is the first to explicitly illuminate their relevance to atomic ionization. Two experiments are presented. In the first we show that the ionization of the electron depends not only on the initial electron energy, but also on the phase space position of the electron with respect to the turnstile–that part of the electron packet inside the turnstile ionizes quickly, after one period of the applied field, while that part outside the turnstile ionizes after multiple kicking periods. In the second experiment we show the signature of the turnstile manifests itself in the step-function-like behavior of the ionization fraction as a function of the kick strength. This behavior persists for different values of kicking periods and starting electron energies.

Acknowledgments

The thesis dissertation marks the end of a long and eventful journey for which there are many people that I would like to acknowledge for their support along the way.

First and foremost, I thank my advisor, Dr. Barry Dunning, for all his guidance and support. His enthusiasm and dedication to research are an inspiration. Deepest gratitude goes to my senior student Brendan Wyker for his patience and his help during the research and the preparation of this dissertation.

My research has benefited from a great number of conversations and collaborations, particularly with Korana Burke, Dr. Kevin Mitchell, Dr. Shuhei Yoshida, Dr. Carlos Reinhold and Dr. Joachim Burgdörfer. Furthermore deep appreciation goes to my other co-workers, Dr. Matt Cannon, Dr. Dean Neufeld, Yu Pu, Changhao Wang, and Vivian Zhang for sharing their sage advice on my work. The time we spent together will never be forgotten - at the lab and beyond work.

Finally, I thank my parents for their support and encouragement throughout my years. They always kept me away from family responsibilities and encouraged me to concentrate on my study.

Contents

Figures

Chapter 1

Introduction

Rydberg atoms, atoms in states of high principal quantum number n, possess unusual properties, including exaggerated responses to electric fields, long orbital periods, and electron wavefunctions that can approximate, specially at very high n, a localized electron in classical orbit about the nucleus. Its dynamics can therefore frequently be described in terms of classical electron orbital motion. The atomic dimensions increase rapidly with n, scaling as n^2. The Rydberg atoms that will be discussed in the following chapters have $n \sim 306$, and hence a valence electron orbit that has a classical diameter of about ~ 10 μm. The classical electron Kepler period scales as n^3, and at $n \sim 300$ is 4.3 ns. Table 1.1 lists several properties of Rydberg atoms and their dependence on n. Even for electrons in a high-n-state, however, low angular momentum orbits penetrate the inner electron core leading to departures from classical scaling. This is especially true in the case of strongly-polarized quasi-one dimensional states, which have large dipole moments.

Quasi-one dimensional states can be produced by photoexcitation of selected Stark states of *very-high-n* (potassium) Rydberg atoms in the presence of a weak dc field. For $m = 0$ states, significant photoexcitation occurs only in the vicinity of the Stark-shifted s, p, and d levels, and those states located near the Stark-shifted d level

Table 1.1 : Scaling properties of Rydberg atoms.

Property	Scaling (a.u.)	$n = 1$	$n = 30$	$n = 306$
Mean-Radius	n^2	5.3×10^{-9} cm	4.8×10^{-6} cm	5.0 μm
Orbital Period	$2\pi n^3$	1.5×10^{-4} ps	4.1 ps	4.3 ns
Binding Energy	$-1/2n^2$	13.6 eV	15 meV	145 μeV
Energy Spacing	$1/n^3$	10.2 eV	1.0 meV	0.94 μeV
Classical Field Ionization Threshold	$1/16n^4$	3.0×10^8 V/cm	400 V/cm	38 mV/cm

have sizable polarizations [15, 33]. Application of a tailored sequence of very short unidirectional pulsed electric fields, termed half-cycle pulses (HCPs), can be used to manipulate and control such states with potential applications ranging from quantum information processing [1] to ultra-cold collisions [2].

If the duration of an HCP is much less than the Kepler orbital period, T_n, it simply delivers an impulsive momentum transfer or "kick" to the electron given by [18]

$$\Delta\vec{p} = -\int \vec{F}_{HCP}(t)dt. \tag{1.1}$$

where $\vec{F}_{HCP}(t)$ is a time-dependent field strength of the HCP(unless otherwise noted, atomic units are used throughout). It can impart energy given by

$$\Delta E = \frac{\Delta\vec{p}^{\,2}}{2} + \vec{p_i} \cdot \Delta\vec{p}\,, \tag{1.2}$$

to the electron, where $\vec{p_i}$ is the initial momentum of the excited electron. This leads to population of a distribution of final states, and, if the energy transfer is sufficient, to ionization. Strong HCPs thus provide the opportunity to study the chaotic ionization of Rydberg atoms subjected to alternating kicks. Such ionization has been the subject of extensive theoretical and experimental interest, which stems both from the use of such pulse trains as a means of controlling the electronic state of atoms and because such systems are excellent models for the study of classical and quantum chaos.

In the present work, we study the ionization of quasi-one-dimensional Rydberg atoms subjected to a periodic sequence of externally applied electric-field pulses that alternate between kicking toward and away from the nucleus. As a periodically driven one-dimensional system, this model exhibits classical chaos, which becomes more rapid as the strength of the kicks increases. The term *turnstile* [3] has been used in the literature to describe a geometric structure in phase space, based on which we analyze the chaotic ionization of this system and the escape process. Current research trends in dynamics place much emphasis on understanding the attractors of a system, but the Hamiltonian systems we are exploring do not have attractors by any reasonable and practical definition of the concept [4]. Therefore, it is important from the point of view of applications to have a different framework for studying chaotic ionization. In other words, we want to motivate many of these issues in chaotic ionization of a Rydberg atom from the viewpoint of problems of *phase space transport*. Besides, we use the idea of stable and unstable manifolds to classify the

orbits on a two-dimensional phase space map. It is a formal mathematical definition of the general notions embodied in the idea of an attractor or repellor in the study of dynamical systems.

Chapter 2 gives some of the basic properties of Rydberg atoms, at the same time elaborating on the theory of quasi-one-dimensional atoms and chaotic transport in dynamical systems. In Chapter 3 a basic description of the experimental apparatus is given. Detailed theoretical results and experimental data are outlined in Chapter 4 followed by a summary and outlook in Chapter 5.

Chapter 2

Rydberg Basics

Since our research is based on potassium Rydberg atoms, it is useful to understand the classical model of a hydrogen-like Rydberg atom. The following text describes the classical behavior of Kèpler orbits in an atomic system, with appropriate quantum corrections when needed. We then discuss the creation and manipulation of quasi-one-dimensional states, following which the general mathematical methods used in chaotic ionization are also introduced.

2.1 Classical Orbital Motion

For understanding the dynamics of the kicked atom experiments, a classical model of the electron orbital motion in an alkali Rydberg atom is very informative. The potential experienced by the single electron in a hydrogen atom is the Coùlomb potential, $V = -1/r$, where r denotes the distance of the electron from the nucleus. It is reasonable to treat the proton as stationary since the mass of a proton is much larger than that of an electron. Hence the origin of coordinates can be set at the nucleus when the resulting Hamiltonian is (in a.u.)

$$H = \frac{\vec{p}^{\,2}}{2} - \frac{1}{r}, \tag{2.1}$$

where $\vec{p}$ denotes the momentum of the electron. The angular momentum $\vec{L} = \vec{r} \times \vec{p}$ is fixed due to the rotational symmetry in this system, which in turn restricts the motion to a plane. By solving the Hamiltonian above for a system with energy $E < 0$, we can get either elliptical or circular orbits. Another conserved quantity in this system

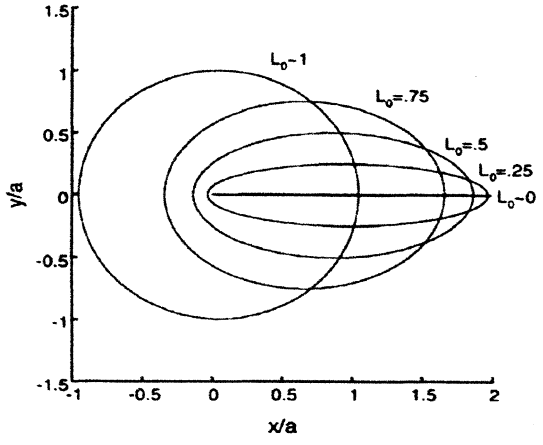

Figure 2.1 : Elliptical orbits of different eccentricities. Low L_0 implies highly elliptical orbits, while high L_0 orbits are near circular [19].

can be inferred from the derivative of the vector $\vec{p} \times \vec{L}$ with respect to t,

$$\frac{d}{dt}\left(\vec{p} \times \vec{L}\right) = \frac{d}{dt}\left(\frac{\vec{r}}{r}\right) \tag{2.2}$$

which says that for the Kepler problem there exists a conserved vector $\vec{A}$, the Runge-Lenz vector, defined by

$$\vec{A} = \vec{p} \times \vec{L} - \hat{r}. \tag{2.3}$$

This vector is in the direction of the radius vector to the perihelion point on the orbit, and has a magnitude that in atomic units is the eccentricity, ε, of the orbit.

We can write down the eccentricity as the term $\varepsilon = \sqrt{1 - 2|E|L^2}$. Since $\vec{A} \cdot \vec{L} = 0$, the Runge-Lenz vector lies in the plane of the orbit, always perpendicular to $\vec{L}$. The vector tells us that, besides being confined to a single plane, the closed elliptical path for the orbit has fixed orientation. By varying the eccentricity, i.e., by varying the Runge-Lenz vector, different elliptical orbits are obtained as shown on Fig. 2.1.

To detail the dynamics in these elliptical orbits, it is convenient to use plane polar coordinates, r, θ, corresponding to $x = r\cos(\theta)$ and $y = r\sin(\theta)$. In a classical picture, the energy of the electron in a Coulomb potential is

$$E = \frac{1}{2}(\dot{r}^2 + r^2\dot{\theta}^2) - \frac{1}{r} = \frac{1}{2}\dot{r}^2 + (\frac{L^2}{2r^2} - \frac{1}{r}), \tag{2.4}$$

where we can define $V_{eff}(r) = \frac{L^2}{2r^2} - \frac{1}{r}$ as a one dimensional effective potential for the radial motion. More important quantities can be expressed in terms of the above results. For example, from Eq. 2.4 we have

$$\dot{r} = \sqrt{2(E - 1/r) - L^2/r^2}, \tag{2.5}$$

by integrating which from the initial state to the state at time t takes the form

$$t = \int_{r_0}^{r} dr \Big/ \sqrt{2(E - 1/r) - L^2/r^2}. \tag{2.6}$$

As it stands, Eq. 2.6 gives t as a function of r and the constants of E, L, and the initial radius r_0. However, it may be inverted, at least formally, to give r as a function of t and the constants [20]. Once the solution for r is found, the solution θ follows immediately from $\theta = Ldt/r^2$, which can be written as

$$\theta = \int_{r_0}^{r} dr \frac{(L/r^2)}{\sqrt{2(E - 1/r) - L^2/r^2}}. \tag{2.7}$$

From this integral we immediately obtain the equation for the closed elliptical path

$$r = \frac{L^2}{1 + \varepsilon \cos\theta}. \tag{2.8}$$

Fig. 2.2 shows an elliptical orbit characterized by different parameters.

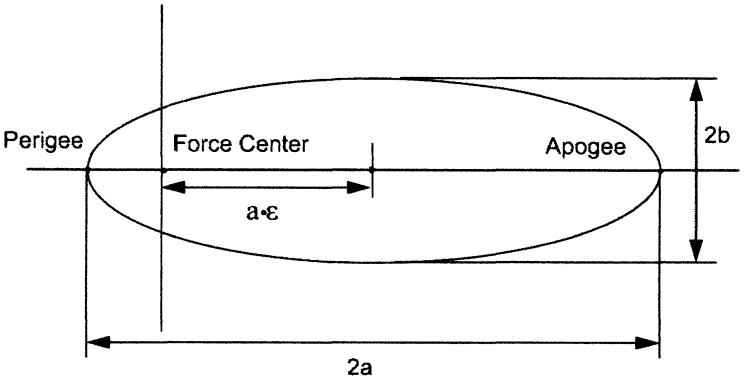

Figure 2.2 : A Kepler orbit and its parameters.

2.2 Stark Effect

It is instructive to describe the Stark effect in hydrogen classically. Comparison of the classical and quantum descriptions can then provide insight to the properties of hydrogen and of classical Keplerian orbits. Moreover, the correspondence between classical and quantum quantities and concepts can be elucidated by such a comparison.

The electron potential in the presence of a static homogeneous electric field E,

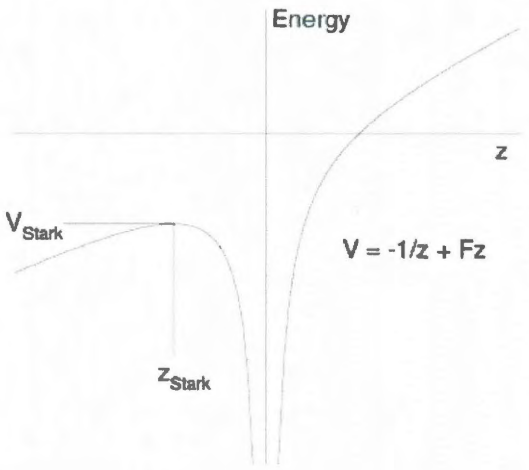

Figure 2.3 : Potential energy for an electron in a uniform, static electric field applied in the z direction.

which is taken to point in the direction of the z axis, becomes

$$V = -\frac{1}{r} + Fz, \tag{2.9}$$

which is shown in Fig. 2.3 for points along the z axis. The Hamiltonian then has the following special form:

$$H = \frac{\vec{p}^{\,2}}{2} + \frac{L^2}{2r^2} - \frac{1}{r} + Fz, \tag{2.10}$$

In quantum mechanics, the shifts in the energy eigenvalues caused by the presence of the field are given in time-independent perturbation theory to first order by,

$$\Delta E_n^{(1)} = F < \Psi_n |\ z\ | \Psi_n >, \tag{2.11}$$

where Ψ_n are the eigenstates of the unperturbed ($F = 0$) Hamiltonian. In second

order the energy shifts are given by

$$\Delta E_n^{(2)} = F^2 \sum_{m \neq n} \frac{| < \Psi_n | \ z \ | \Psi_m > |^2}{E_n - E_m}, \tag{2.12}$$

where E_n and E_m are the eigenvalues of the unperturbed Hamiltonian. The continuum should be included on the right-hand side of Eq. 2.12, so we replace the sum by an integral above the continuum threshold [5]. The energy shifts Eq. 2.12 are closely connected with the dipole polarizability of the atom in an electric field. Eq. 2.11 can describe the modifications to the wave functions caused by an infinitesimally weak electrical field. Thus the modified eigenfunctions can be written as

$$|\Psi_n' >= |\Psi_n > + F \cdot \sum_{m \neq n} \frac{< \Psi_n | \ z \ | \Psi_m >}{E_n - E_m} | \Psi_m > . \tag{2.13}$$

These functions have a dipole moment that is induced by the external field and that points along the z axis. Assuming $\Delta E_n^{(1)} = 0$, the z-component of the induced dipole moment is

$$\begin{aligned} d_z &= - < \Psi_n' | \ z \ | \Psi_n' > \\ &= 2F \sum_{m \neq n} \frac{| < \Psi_m | \ z \ | \Psi_n > |^2}{E_m - E_n} \\ &\equiv \alpha_d F. \end{aligned} \tag{2.14}$$

Using the dipole polarizability α_d we can write the energy shift for the state ψ_n resulting in a quadratic Stark effect as

$$\Delta E_n^{(2)} = -\frac{\alpha_d}{2} F^2. \tag{2.15}$$

Classically field ionization is possible when the electron energy lies above the saddle point in the potential. Eq. 2.9 and Fig. 2.3 show that for a one-electron potential, the Stark saddle point is located on the negative z axis at the local maximum of V. The position z_s and energy V_s of the saddle point are

$$z_s = -1/\sqrt{F},\ V_s = -2\sqrt{F}. \tag{2.16}$$

It is possible in parabolic coordinates to separate the Schrödinger equation into ordinary differential equations, even in the presence of an external electric field. As the electric field in the z direction does not disturb the rotational symmetry around the z axis, it is sensible to keep the azimuthal angle Ψ as one of the coordinates. The two other coordinates ξ and η have the physical dimension of a length and are defined by

$$\begin{aligned} \xi &= r + z, \\ \eta &= r - z, \\ z &= \frac{\xi - \eta}{2}, \\ r &= \frac{\xi + \eta}{2}. \end{aligned} \tag{2.17}$$

The coordinates ξ and η can assume values between zero and $+\infty$. They are called parabolic, because surfaces defined by $\xi = const$ and $\eta = const$ are paraboloids of rotation around the z axis.

We can rewrite the Hamiltonian in parabolic coordinates as

$$H = -\frac{2}{\xi+\eta}\frac{\partial}{\partial\xi}\left(\xi\frac{\partial}{\partial\xi}\right) - \frac{2}{\xi+\eta}\frac{\partial}{\partial\eta}\left(\eta\frac{\partial}{\partial\eta}\right) - \frac{1}{2\xi\eta}\frac{\partial^2}{\partial\phi^2} - \frac{2}{\xi+\eta} + F\frac{\xi-\eta}{2}. \tag{2.18}$$

Then we can apply the separation of variables technique, assuming the solution has the form,

$$\psi(\xi,\eta,\phi) = u_1(\xi)u_2(\eta)e^{im\phi}. \tag{2.19}$$

obtaining two decoupled equations for $u_1(\xi)$ and $u_2(\eta)$

$$\frac{d}{d\xi}\left(\xi\frac{du_1}{d\xi}\right) + \left(\frac{E\xi}{2} + Z_1 - \frac{m^2}{4\xi} - \frac{F\xi^2}{4}\right)u_1 = 0 \tag{2.20}$$

and

$$\frac{d}{d\eta}\left(\eta\frac{du_2}{d\eta}\right) + \left(\frac{E\eta}{2} + Z_2 - \frac{m^2}{4\eta} - \frac{F\eta^2}{4}\right)u_2 = 0 \tag{2.21}$$

There are two separation constants, Z_1 and Z_2, which are related by

$$Z_1 + Z_2 = 1. \tag{2.22}$$

Using associated Laguerre polynomials the wavefunctions can be written as

$$\psi_{nn_1n_2m} \propto e^{im\phi}\xi^{n_1+\frac{|m|}{2}}\eta^{n_2+\frac{|m|}{2}}e^{-\frac{(\xi+\eta)}{2n}} \tag{2.23}$$

Transforming this expression into polar coordinates results in the electronic probability distribution [21]

$$|\psi_{nn_1n_2m}|^2 = r^{2n-2}(1+\cos\theta)^{2n_1+|m|}(1-\cos\theta)^{2n_2+|m|}e^{-2r/n}. \tag{2.24}$$

This probability density is plotted for $n = 8$, $m = 0$, $n_1 - n_2 = -7$ to 7 in Fig. 2.4.

In the field-free case $F = 0$, Eq. 2.21 has the same form as Eq. 2.20. In the negative energy regime there is a discrete sequence of energies, namely $E_n = -1/(2n^2)$, $n = 1, 2, ...$, at which both equations 2.20 and 2.21 with appropriate values of Z_1 and Z_2

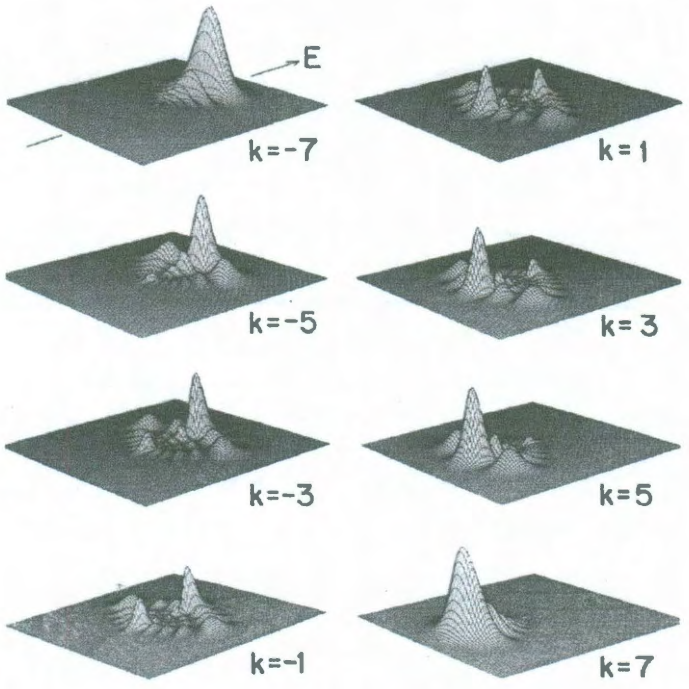

Figure 2.4 : Charge distribution for the parabolic eigenstates of H : $n = 8, m = 0, k = n_1 - n_2 = -7$ to $+7$. The asymmetry of the charge distribution for the extreme Stark states leads to a permanent dipole moment [21].

simultaneously have square integrable solutions with n_1 and n_2 nodes respectively. The parabolic quantum numbers $n_1 = 0, 1, 2, ...$ and $n_2 = 0, 1, 2, ...$ are related to Z_1, Z_2 and the principal quantum number n for a given azimuthal quantum number $m = 0, \pm 1, \pm 2, ... \pm (n-1)$ by

$$n = n_1 + n_2 + |m| + 1, \tag{2.25}$$

$$Z_1 = \frac{1}{n}\left(n_1 + \frac{|m|+1}{2}\right), \tag{2.26}$$

and

$$Z_2 = \frac{1}{n}\left(n_2 + \frac{|m|+1}{2}\right). \tag{2.27}$$

If the field strength F is non-vanishing (positive), then Eq. 2.21 can be solved for a given value of the separation constant $Z_2(= Z - Z_1)$ and any energy with the appropriate boundary conditions. The solutions $u_2(\eta)$ do not behave like regular or irregular Coulomb functions asymptotically, because the potential decreases linearly with z, i.e., the kinetic energy increases linearly with η.

The classical dipole moment can be deduced in the following way. Averaged over a Kepler period the direction of the dipole moment will point toward the pericenter of the orbit, $\hat{A}$. From the definition of the dipole moment, we know that it is related to the electron position, hence its average magnitude over a period has the form,

$$\begin{aligned}
|\langle\vec{d}\rangle| &= \frac{1}{\tau}\int_0^\tau r\cos\theta\,\mathrm{d}t \\
&= \frac{1}{2\pi n^3}\int_{-\pi}^{\pi} r\cos\theta\,\frac{1}{\dot{\theta}}\,\mathrm{d}\theta \\
&= \frac{1}{2\pi n^3}\int_{-\pi}^{\pi} \frac{r^3}{r^2\dot{\theta}}\cos\theta\,\mathrm{d}\theta \\
&= \frac{L^5}{2\pi n^3}\int_{-\pi}^{\pi} \frac{\cos\theta}{(1+\varepsilon\cos\theta)^3}\,\mathrm{d}\theta \\
&= \frac{3}{2}n^2\varepsilon.
\end{aligned} \tag{2.28}$$

in spherical coordinates (r, θ, φ).

2.3 Quasi-1D Atoms

In this work we study strongly polarized quasi-1D Rydberg atoms. While such atoms provide a simple and convenient model to test advanced mathematical tools, another reason to study these atoms is that techniques for controlling and manipulating such atoms are allowing the creation of well defined wavepackets that can be developed, trapped, focused, and steered into desired regions of phase space [24]. In the past few years, work has been done for developing experimental techniques for creating highly excited quasi-1D Rydberg atoms and then subjecting such atoms to a variety of periodic pulse sequences [6]. Moreover, such work demonstrates using classical trajectory Monte Carlo (CTMC) simulations, that many of the essential features of the experiments on quasi-1D Rydberg atoms can be modeled using purely 1D simulations along a radial half-line [7].

The extreme members of low-$|m|$, high-n Stark manifolds have large permanent dipole moments and approximate quasi-1D states [15]. Eq. 2.9 is the Hamiltonian of this system. For weak dc fields, its eigenvectors $|\alpha\rangle$ (i.e., $H|\alpha\rangle = \varepsilon_\alpha|\alpha\rangle$) can be calculated using an expansion

$$|\alpha\rangle = \sum_{n,\ell} a^{\alpha}_{n,\ell}|n,\ell\rangle, \tag{2.29}$$

in a spherical alkali state basis consisting of the bound eigenstates $|n,l\rangle$ of H_{at}, the field-free atomic Hamiltonian, where $H_{at}|n,l\rangle = E_{nl}|n,l\rangle$.

Fig. 2.5 shows us the Stark spectrum for K($m = 0$) states in the vicinity of $n = 50$. However, in this work, experiments are performed for $n = 306$ or $n = 350$. The reason

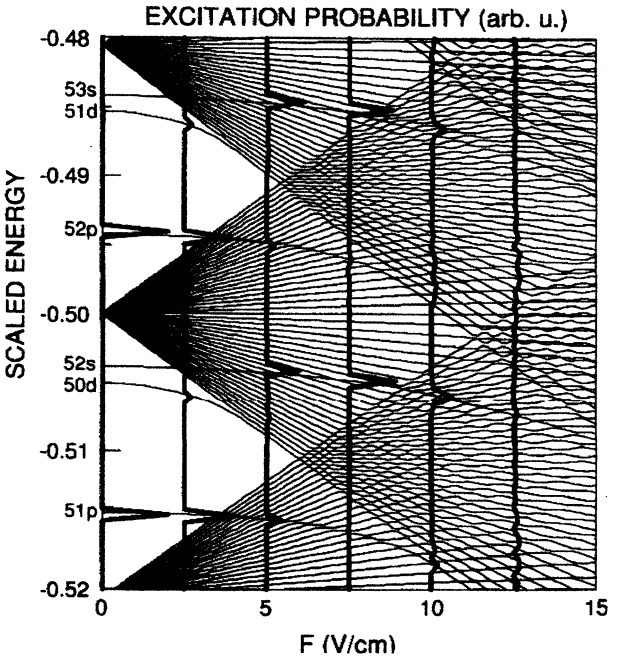

Figure 2.5 : Calculated Stark energy level structure for K($m = 0$) states in the vicinity of $n = 50$ (thin lines). Also included is the probability for photoexcitation from the ground state (thick lines) by a laser with a linewidth $\Delta\omega_L = 10^{-3}/n^2$ for different values of applied DC field. Energies are displayed in scaled units $\epsilon_0 = n^2\epsilon$ [15].

of not showing their manifolds is because it is difficult to graphically resolve all states for $n > 300$ due to the fact that the number of Stark states per manifold increases as n. However, the general characteristics of the overall Stark level structure are largely independent of n.

The discussion of the behavior at very high n can be based on the Stark map in Fig. 2.5. We can see that due to large quantum defects ($\mu_s = 2.19, \mu_p = 1.71$), as the applied dc field is increased, the s and p states initially encounter states in neighboring Stark manifolds of different n, whereas d states which have a small quantum

defect ($\mu_d = 0.25$) first encounter Stark states of the same n. As a d state approaches its neighboring manifold, strong mixing leads to the appearance of a broad avoided crossing, the initial state correlating adiabatically with the extreme lowest-energy, redshifted "downhill" Stark states. These states are highly polarized, so play an important role in realizing the quasi-1D states. To detail this idea in a more theoretical way, we define a laser pulse $F_L(t) = L(t)cos(w_L t)$ along the z axis. This laser pulse can create a Rydberg wave packet with a wave function,

$$|\psi_e xcit(t)\rangle = C\sum_\alpha W_{\alpha i}|\alpha\rangle e^{-i\varepsilon_\alpha t}, \tag{2.30}$$

where C is a normalization constant. In first order perturbation,

$$W_{\alpha i} \approx -\frac{i}{2}\int_{-\infty}^{+\infty} dt L(t) e^{-i\omega_L t} e^{i(\varepsilon_\alpha - \varepsilon_i)t}\langle\alpha|z|i\rangle = -\frac{i}{2}\tilde{L}(\omega_{\alpha i} - \omega_L)\langle\alpha|z|i\rangle,$$

where rotating wave approximation is used and $\omega_{\alpha i} = \varepsilon_\alpha - \varepsilon_i$ and $\tilde{L}(\omega - \omega_L)$ is the Fourier transform of $L(t)$. Then we can write down the probability for photoexcitation of ground-state potassium atoms,

$$P_{excit}(\varepsilon) = \frac{1}{4}\sum_\alpha |\tilde{L}(\varepsilon_\alpha - \varepsilon)|^2 |\langle\alpha|z|i\rangle|^2. \tag{2.31}$$

Dipole coupling dictates that transitions obey the selection rule $\langle n'\ell'|z|n\ell\rangle \sim \delta_{\ell,\ell\pm1}$ which given that the ground state of potassium is $|i\rangle = |4s\rangle$ leads to

$$|\langle f|z|4s\rangle|^2 = \left|\sum_n \alpha_{np}^f \langle np|z|4s\rangle\right|^2 \cong |\langle\overline{np}|z|4s\rangle|^2 \left|\sum_n \alpha_{np}^f\right|^2, \tag{2.32}$$

where $\langle f|$ is the final state of the transition. We use an approximation that for large n values $\langle np|z|4s\rangle$ is independent of n for the above equation.

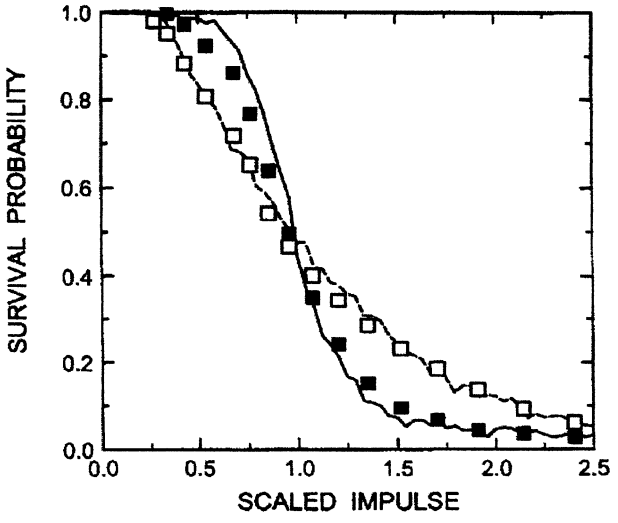

Figure 2.6 : Survival probabilities for quasi-1D atoms in low lying states in the $n = 350$ manifold as a function of scaled momentum. Closed squares represent experimental data for HCPs applied transverse to the axis of the atom, while open squares represent data for HCPs applied along the axis. Lines represent CTMC simulations [22].

Experimental verification of the production of quasi-1D states has already been achieved. Based on the reference [22], fig. 2.6 illustrates the experimental results. With the probe impulses applied along the atomic axis, the rate of decrease of the survival probability with increasing probe impulse is significantly less than with the probe impulse applied transverse to the atomic axis. In other words, the width of the electron momentum distribution transverse to the atomic axis is substantially smaller than that parallel to the axis, which is an evidence of the production of quasi-1D states.

2.4 Chaotic Transport in Dynamical System[1]

Dynamics is the study of how systems change in time. The ultimate goal of this work is testing the application of theories of dynamics to atomic systems. As a starting point, it is necessary to introduce the basic concepts of stable manifolds and unstable manifolds.

For a system that either is an iterated function or has discrete-time dynamics, we can have the following definitions. Let X be a topological space, and $f : X \rightarrow X$ a homeomorphism. If p is a fixed point for f, the stable set of p is defined by

$$W^s(f,p) = q \in X : f^n(q) \; as \; n \rightarrow \infty \tag{2.33}$$

and the unstable set of p is defined by

$$W^u(f,p) = q \in X : f^{-n}(q) \; as \; n \rightarrow \infty. \tag{2.34}$$

Here, f^{-1} denotes the inverse of the function f, i.e. $f \circ f^{-1} = f^{-1} \circ f = id_X$, where id_X is the identity map on X. To detail it more clearly in Fig. 2.7, p_j is a fixed point for an unstable manifold. We know that this manifold is unstable because the arrows indicate that points on the curve will move away from the fixed point along the manifold if mappings are applied to them. Alternately, p_i is the fixed point for the stable manifold $W^s(p_i)$ because arrows indicate that mappings can cause the points on the manifold converge into the fixed point eventually.

[1] Much of the discussion in this section follows that of Wiggins [4].

The system we discuss in this work is time-dependant perturbation of a planar (hence completely integrable) Hamiltonian system. This research is limited to the case where the perturbation is periodic in time. And we study the perturbed system using the associated Poincaré map obtained by considering the discrete motion of points after time intervals of one period of the perturbation under the dynamics of the trajectories of the perturbed vector field. Throughout this chapter two general ideas are exploited.

1. We study the boundaries between regions of qualitatively different types of motion formed by segments of stable and unstable manifolds of hyperbolic periodic orbits (or, possibly, cantori).

2. To completely describe the transport between the different regions of phase space separated by stable and unstable manifolds, we use the dynamical evolution of certain segments of the stable and unstable manifolds, the so-called *turnstiles*.

As our dynamical system we consider a C^r $(r \geq 1)$ homeomorphism

$$f : M \to M, \tag{2.35}$$

where M is a differentiable (C^r, $r \geq 1$), orientable, two-dimensional manifold, e.g., the plane, a sphere, the cylinder, a torus, but not a Klein bottle. We will use pieces of $W^s(p_i)$ and $W^u(p_j)$ to partition M into disjoint regions to study transport between them, but first we need a few definitions.

Definition. *A point $q \in M$ is called a heteroclinic point if $q \in W^s(p_i) \cap W^u(p_j)$ for*

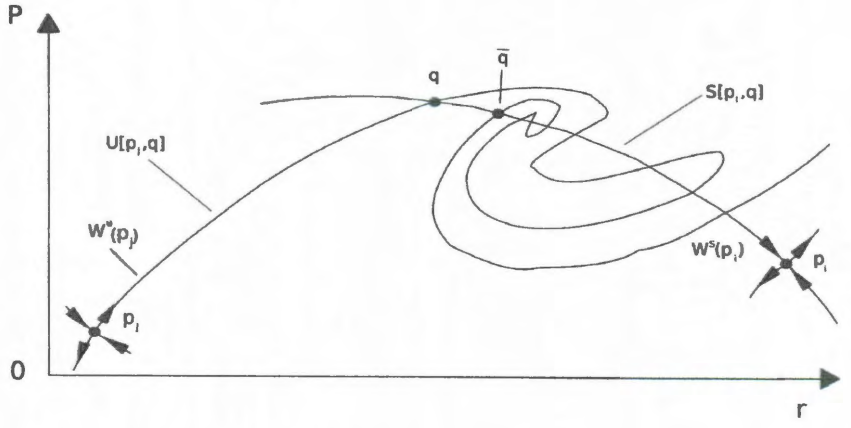

Figure 2.7 : q is a pip, $\bar{q}$ is not a pip.

some p_i, p_j if $i \neq j$. If $i = j$, then q is called a homoclinic point.

As we develop the transport theory, certain homoclinic and heteroclinic points will play a distinguished role.

Definition. *Suppose $q \in W^s(p_i) \cap W^u(p_j)$, and let $S[p_i, q]$ denote the segment of $W^s(p_i)$ with endpoints p_i and q and $U[p_j, q]$ denote the segment of $W^u(p_j)$ with endpoints p_j and q. Then q is called a primary intersection point (pip) if $S[p_i, q]$ intersects $U[p_j, q]$ only at the point q (and p_i if $i = j$); see Fig. 2.7.*

In other words, stable manifold $W^s(p_i)$ intersects with unstable manifold $W^u(p_j)$ at q and $\bar{q}$ giving this manifold at least two pips. The next two definitions provide us with convenience to discuss the dynamics on a phase space.

Definition. *Suppose $q_0, q_1 \in W^s(p_i)$ and that q_1 is closer than q_0 to p_i in the sense of arclength along $W^s(p_i)$. Then we say that $q_1 <_s q_0$. Similarly, suppose that $q_0, q_1 \in$*

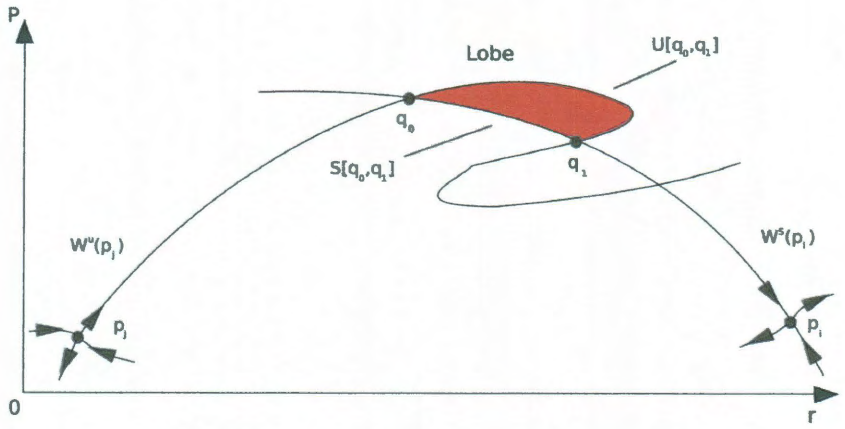

Figure 2.8 : The definition of a lobe with $q_0 <_u q_1$ and $q_1 <_s q_0$.

$W^u(p_j)$ *and that* q_0 *is closer than* q_1 *to* p_j *in the sense of arclength along* $W^u(p_j)$. *Then we say that* $q_0 <_u q_1$; *see Fig. 2.8.*

Definition. *Let* $q_0, q_1 \in W^s(p_i) \cap W^u(p_j)$ *be two adjacent pips, i.e., there are no other pips on* $U[q_0, q_1]$ *and* $S[q_0, q_1]$, *the segments of* $W^u(p_j)$ *and* $W^s(p_i)$ *connecting* q_0 *and* q_1. *Then we refer to the region interior to* $U[q_0, q_1] \cup S[q_0, q_1]$ *as a lobe; see Fig. 2.8.*

Suppose $W^s(p_i)$ and $W^u(p_j)$ intersect in the pip q. In Fig. 2.8 we can see several lobes form interesting geometries on the space. Several Lemmas are needed before we further study the behavior of transport.

Lemma. *Suppose* $q_0, q_1 \in W^s(p_i)$ *with* $q_0 <_s q_1$; *then* $f^k(q_0) <_s f^k(q_1)$ *for all* $k \in \boldsymbol{Z}$. *Similarly, suppose* $\bar{q}_0, \bar{q}_1 \in W^u(p_j)$ *with* $\bar{q}_0 <_s \bar{q}_1$; *then* $f^k(\bar{q}_0) <_s f^k(\bar{q}_1)$ *for all* $k \in \boldsymbol{Z}$.

Lemma. *Suppose* $q \in W^s(p_i) \cap W^u(p_j)$ *is a pip; then* $f^k(q)$ *is a pip for all* $k \in \boldsymbol{Z}$.

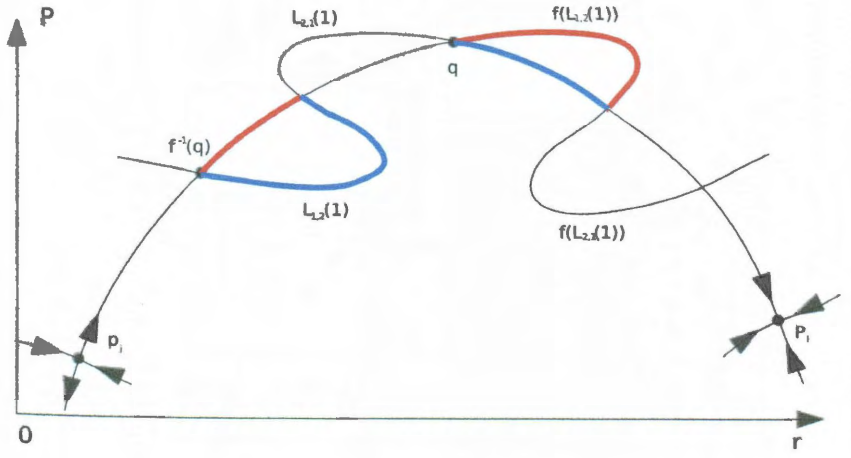

Figure 2.9 : The dynamics of the lobes.

We shall discuss the conclusion resulted from the two lemmas above in Fig. 2.8. According to these two lemmas, all the points along one manifold can only be transported by mappings with preservation of their original orders and orientations. The direct result is that the red segment with one endpoint $f^{-1}(q)$ in Fig. 2.9 will become the red segment with one endpoint q after one mapping. Similarly, the two blue segments in Fig. 2.9 are exchangeable by one mapping or the inverse of one mapping. Since the lemmas do not talk about points other than those on the manifolds, the question lies in where the points inside one lobe will be transported after one mapping. Based on the continuity, it is easy to prove that [4] points in the lobe $L_{1,2}(1)$ can not be transported to the area above the $W^u(p_j)$ (the red area in Fig. 2.10.) Otherwise, if we connect an arbitrary point in $L_{1,2}(1)$ and an arbitrary point on the adjacent blue segment with a curve within the lobe, we will find that, after one map-

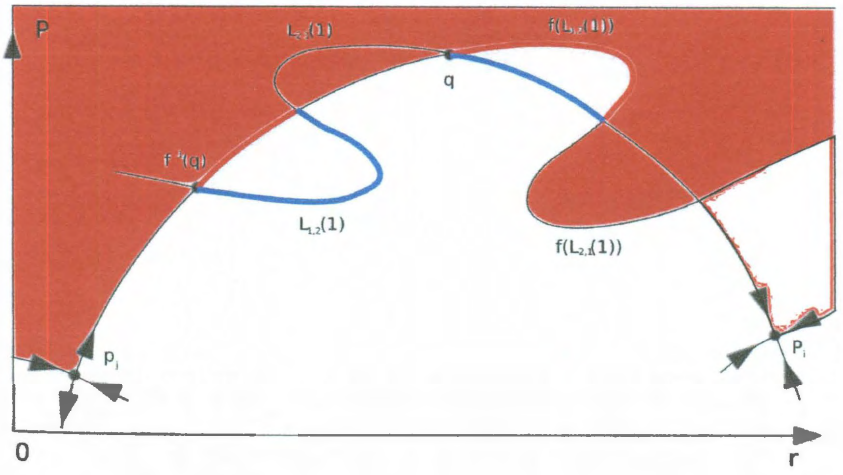

Figure 2.10 : Forbidden area of transportation I.

ping, the image of this curve will go across the red segment surrounding $f(L_{1,2}(1))$ if that arbitrary point in $L_{1,2}(1)$ is transported to the red area. And this violates the two lemmas above, because the pre-image of the intersection point between the curve and the red segment should lie on the red segment surrounding one side of $L_{1,2}(1)$ rather than inside of $L_{1,2}(1)$. For the same reason, points in the lobe $L_{1,2}(1)$ can not be transported to the area below the $W^s(p_i)$ (the blue area in Fig. 2.11; the purple areas are the overlap between the red area and blue area.)

Fig. 2.10 draws a conclusion of this section. After one mapping, points in $L_{1,2}(1)$ can be only transported to $f(L_{1,2}(1))$, and similarly points in $L_{2,1}(1)$ to $f(L_{2,1}(1))$. The two lobes $L_{1,2}(1)$ and $L_{2,1}(1)$ have been called a turnstile by mathematicians [3]. In other words, all the points from a turnstile are mapped into the next turnstile.

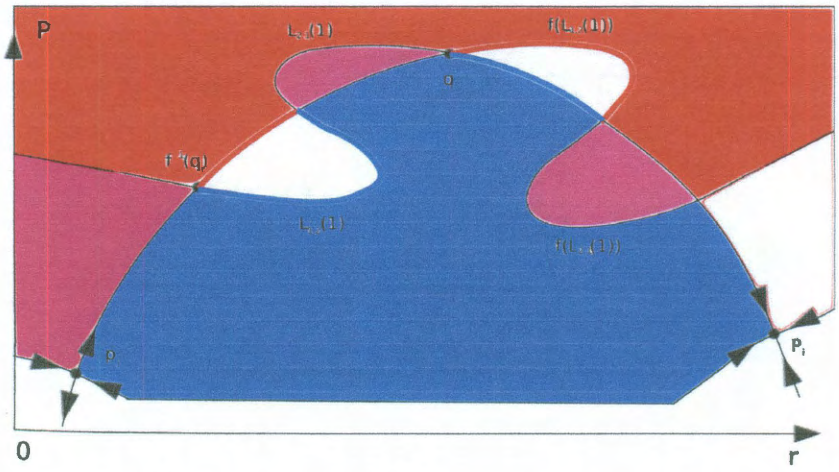

Figure 2.11 : Forbidden area of transportation II.

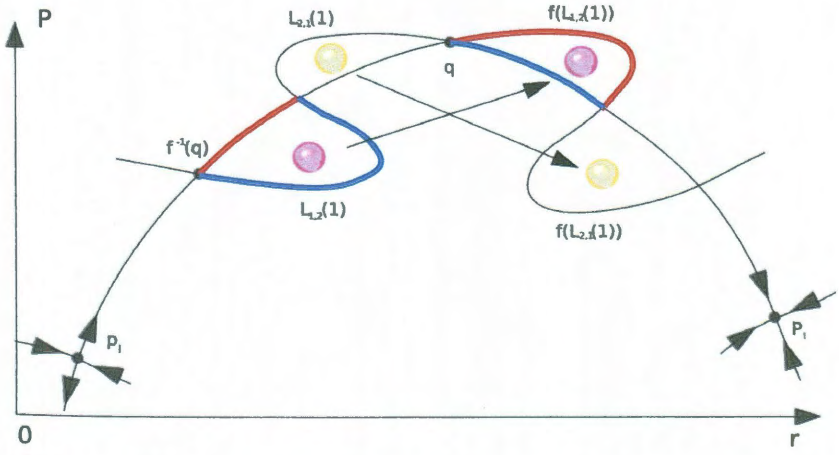

Figure 2.12 : Tranportation between lobes.

Chapter 3

The Experimental Apparatus

The current experimental set up has been developed over several years to allow detailed study of very-high-n Rydberg atoms. It includes a vacuum system, a laser system and a collection of fast pulse generators to apply the necessary HCPs. To eliminate collisions with air molecules, experiments are undertaken in a diffusion-pumped vacuum chamber. Rydberg atoms are created by photo excitation of potassium atoms contained in a collimated beam using the crossed output of an extra cavity-doubled Rh6G dye laser. The atomic beam intersects the laser beam in an interaction region which comprises three pairs of copper plate electrodes arranged as a cube. Experiments are conducted in a pulsed mode. The output of the dye laser is chopped by an acousto-optic modulator into a train of $1\mu s$-duration pulses. Following excitation, the atoms are subject to a sequence of carefully tailored half-cycle pulses (HCPs) produced by combining the outputs from several pulse generators and applying the resulting waveform to a nearby electrode. Following a delay of $5-10\mu s$, the number and n-state distribution of the surviving Rydberg atoms is determined by selective field ionization (SFI), in which a linearly increasing ionization field is applied. A channel electron multiplier is used to detect electrons produced by field ionization. Measurements in which no HCPs are applied are interspersed uniformly throughout

data acquisition to monitor the number of Rydberg atoms initially created by laser excitation. We determine the survival probability by calculating the ratio of the number of Rydberg atoms detected with and without HCPs applied. The timing sequence for a typical experiment is: (1) Photoexcite Rydberg atoms, (2) Apply the HCPs, and (3) Detect the surviving atoms. The main body of the apparatus is shown on Fig. 3.1.

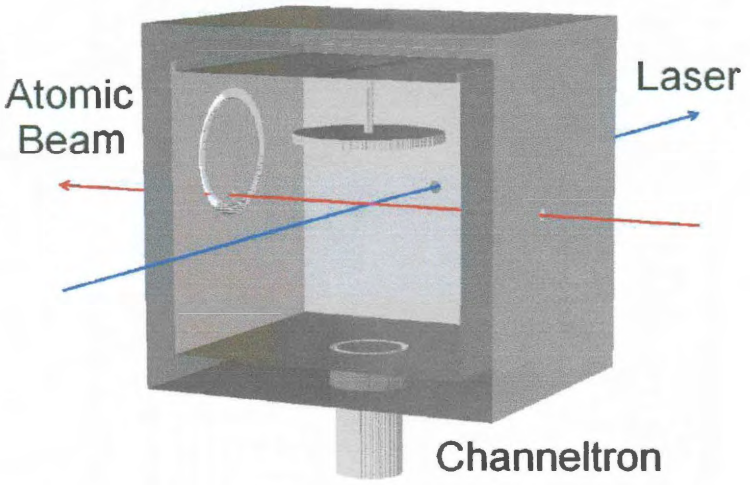

Figure 3.1 : Diagram of the modified apparatus with the front face removed for illustrative purposes. A UV laser pulse intersects a collimated alkali beam exciting high-n Rydberg states. Half-cycle electric field pulses (HCPs) and electric field steps are applied by the two electrodes, while the channeltron electron multiplier measures electrons resulting from field ionization.

3.1 The Laser System

The laser system consists of a Verdi V8 solid state laser, a Rh6G Coherent 699-21 single frequency dye laser and a Spectra-Physics Wavetrain tunable CW frequency doubler. The typical output power of the dye laser is about $1W$ if pumped by $7.5W$ of $532nm$ light from the Verdi laser. The laser can generate radiation with wavelengths of about $528.7nm$, which after being frequency doubled can excite the potassium $4s$ ground state to Rydberg states with $n \sim 306$.

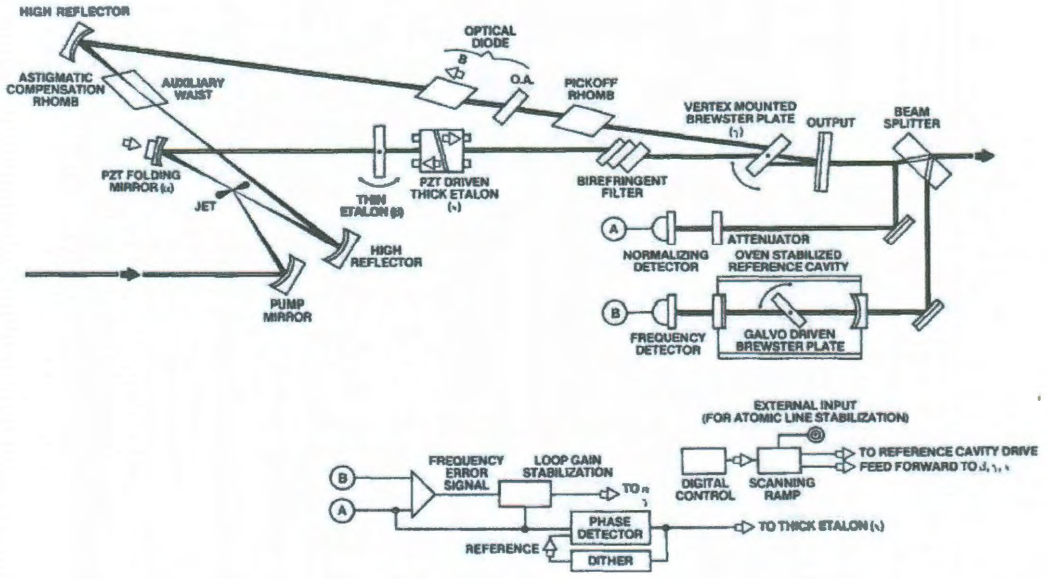

Figure 3.2 : The ring laser cavity is formed by four mirrors: three high reflectors and the output mirror. Details of tuning and operation are explained in Ref. [11, 26, 27]. This diagram is taken from [11]

Fig. 3.2 shows the ring dye laser schematic. The dye laser ring is produced by a pump laser beam and a laminar jet stream formed by a carefully designed stainless

steel nozzle. The problem of astigmatism which normally occurs in a ring laser cavity is solved in Coherent's CR-699 by a silica rhomb placed near the ring laser's auxiliary beam waist. A reference cavity, including a Fabry-Perot interferometer and a galvo driver Brewster plate, creates error signal which is transmitted to an AGC (automatic gain control) circuit unit. Its output goes into a frequency cross over circuit, where the error signal is separated into high frequency component and low frequency component. The HF component is fed back to a PZT fold mirror that can lower the frequency jitter to about 250 kHz, while the LF component controls a vertex-mounted Brewster plate in the laser cavity that can only respond to signals below 120 Hz. A 3-plate birefringent filter provides a broad bandpass with bandwidth of 380 GHz. Together with a thin etalon with a 200 GHz FSR, and thick etalon with a 10 GHz FSR, the effective output line width can be narrowed down to less than 500 kHz.

The Wavetrain frequency-doubler uses a BBO crystal in a ring configuration and the Pound-Drever active resonator stabilization method to provide a doubling efficiency of 5-10% over a large spectral range [30, 31]. The configuration of the cavity is a compact triangle shape, which can ensure high efficiency and stability to vibrations and acoustic noise. The output laser beam of the doubler goes through an acousto-optic modulator (AOM), where the beam is chopped into short pulses, usually of $1\mu s$ duration. AOMs are also termed Bragg cells, using the acousto-optic effect to diffract and shift the frequency of light using sound waves (usually at radio-frequency). A piezoelectric transducer is attached to a material such as glass. An oscillating electric

signal drives the transducer, which creates sound waves in the glass. These can be thought of as moving periodic planes of expansion and compression that change the index of refraction. Incoming light scatters off the resulting periodic index modulation and interference occurs similar to Bragg diffraction. The amount of light diffracted by the sound wave depends on the intensity of the sound. Hence, the intensity of the sound can be used to modulate the intensity of the light in the diffracted beam. Typically, the intensity of the m = 1 order can be varied between 0% and 80%, by varying the amplitude of the drive field.

A scanning Michelson interferometer is used to monitor the dye laser wavelength [29]. This utilizes two retroreflecting corner cubes mounted on a moving carriage and counts the fringes seen at the dye laser wavelength and compares this number to the fringe count for a polarization-stabilized HeNe laser. Its accuracy can reach ±1GHz at the operating wavelength.

To increase the long term stability of the dye laser, a Superlock system is used to lock the dye laser frequency to an ultrastable commercial stabilized HeNe laser via a confocal Fabry-Perot etalon [28]. As we need to scan the laser to pinpoint the state of large dipole moment, the dye laser can also be scanned using Superlock over a 500MHz frequency interval while maintaining a reproducibility of +/− 1MHz from scan to scan.

3.2 The Vacuum Chambers

The vacuum system comprises two chambers pumped by Varian VHS-6 and VHS-4 diffusion pumps producing a vacuum of $\sim 5 \times 10^{-8}$ Torr in the experimental volume. The vacuum is monitored by Bayard-Alpert ionization gauges located in each chamber.

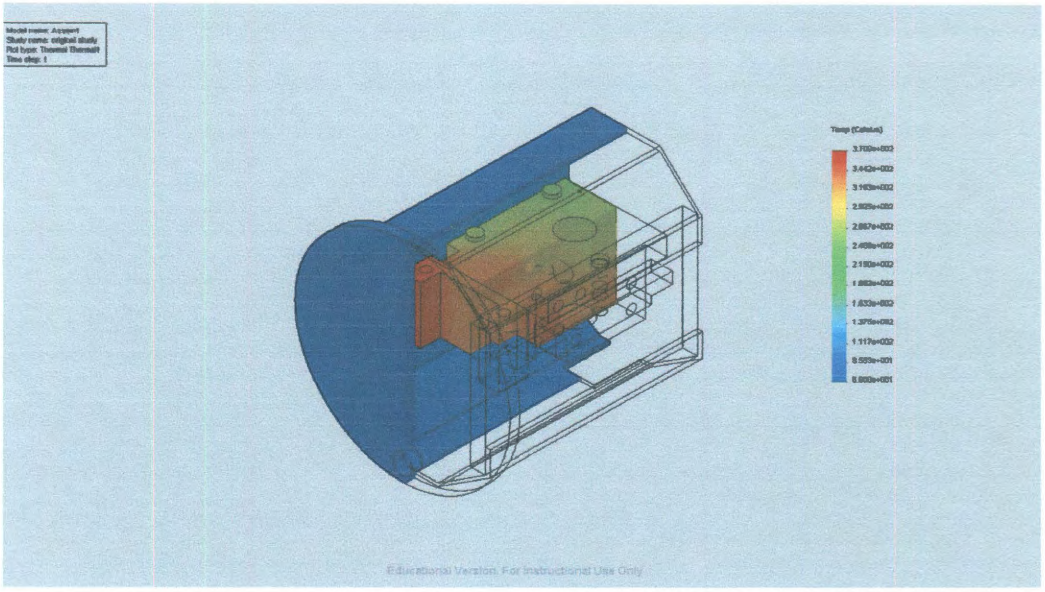

Figure 3.3 : Simulation of the current oven design.

The potassium beam oven rests in the source chamber. It contains a 5g ampoule of potassium. In order to prevent potassium from clogging the nose aperture, we have to maintain the temperature difference between the nose and the body. As shown on Fig. 3.3, the body of the oven is heated to 315 °C by applying current to resistive heater cartridges inserted into the oven body while the nose is heated to 365 °C. This

simulation is done by using SolidWorks to perform a finite element analysis on a model resembling the real part.

The potassium exits the oven through a 0.38 mm aperture in the nose and travels approximately 10 cm before passing through the 0.7 mm collimating aperture at the entrance to the main chamber and interaction region. A rough estimate of the beam's angular divergence may then be calculated using the expression

$$\theta_d = 2arctan\Big(\frac{d_f - d_i}{2l}\Big), \tag{3.1}$$

where θ_d denotes the angular divergence, d_f and d_i denote the diameters of the two apertures, and l denotes the distance between the apertures. With the values given the angular divergence is estimated to be $\sim 0.2°$. Then the atomic beam intersects the laser beam in the interaction region.

3.3 The Interaction Region and Detection

The interaction region consists of three pairs of planar copper plate electrodes. Small potentials applied to these plates are used to cancel stray background fields, and to establish offset fields. The top and bottom plates produce the offset field in the z direction. HCPs are generated by applying voltage pulses to the small inset electrodes. HCPs along the z direction, are produced using a 2" diameter, $\frac{1}{8}$" thick disk electrode mounted from the top plate on a piece of semi-rigid coax cable and is terminated by $50\,\Omega$ resistor. This electrode is biased to the same potential as the top plate.

Below the interaction region lies a Sjuts Optotechnik KBL 25RS channel electron

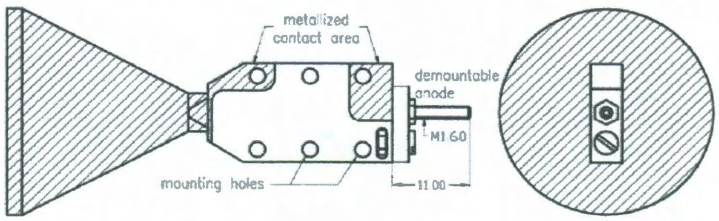

Figure 3.4 : Sjuts Optotechnik KBL 25RS channeltron electron multiplier schematic. The channeltron is used to detect electrons resulting from Rydberg atom ionization.

multiplier (Fig. 3.4) [32]. It contains a long biased channel that multiplies incident charges through an avalanche that can be triggered by any charged particle hitting the bell-mouthed entrance cone with sufficient energy to cause secondary emission. Using this multiplier we can realize the selective field ionization (SFI) technique, which not only allows measurement of the number of surviving Rydberg atoms, but also gives information about the excited state energy distribution. Because atoms in different Rydberg states ionize at different applied fields, measurement of the ionization signal as a function of the applied field during a linearly increasing electric field can provide information on the energy distribution of the atoms present at the time of application of the field [14]. In practice a linearly-increasing voltage ramp is applied to the lower plate and the electron arrival time distribution is measured. Previous work [23] shows that free electrons produced by HCP-induced ionization can reside in the interaction region for survival microseconds and can be counted in the SFI spectrum. Hence we leave a time delay between the time of HCP application and the time of SFI extraction

to allow the free electrons time to drift from the interaction region.

3.4 Electric Field Pulses

The pulse generators used in this experiment are a Picosecond Pulse Labs (PSPL) 10,050 pulser and two Hewlett-Packard (HP) 8131A pulsers. The PSPL 10,050 provides a single pulse used as the "up" pulse in the experiment, which will be detailed in Chapter 4. The pulse rise time is 45ps and fall time is 110ps, with pulse duration of 600ps. The amplitude is adjusted using broadband attenuators with a bandwidth of DC to 6GHz. The HP generators are GPIB-controllable. One of them pulses the "down" kicks, while the other one generates a pre-pulse. The widths of their pulses are both 600ps. These pulse generators are triggered by a Stanford Research Systems DG535 Digital Delay Generator with 5 ps resolution.

Chapter 4

Chaotic Transport in a Hydrogen Atom Exposed to Alternating Kicks

As discussed in Chapter 2, using the turnstile technique an analysis of the lobe structure can be performed. After demonstrating that the ionization process here is governed by a phase-space turnstile, we study the geometry of the lobes of the turnstile. Experimentally accessible kicking parameters can determine the size, shape, and position of these lobes. In particular, we investigate this by varying the kick duration, kick strength, and kicking period. Two experiments have been done to explore the influence of the lobe dynamics on the ionization process. In the first experiment, a highly excited n=350 energy eigenstate is subjected to a single kicking cycle, immediately after which the ionization fraction is measured. In the second experiment, we expose a nonstationary electronic state that is first maneuvered into a given region of phase space to a train of alternating kicks. After each kicking period, the survival probability is recorded. We find that the survival probability is highly sensitive to whether the initial placement of the state in phase space is within the turnstile lobe. If so, it yields rapid ionization.

4.1 Theoretical Scheme[1]

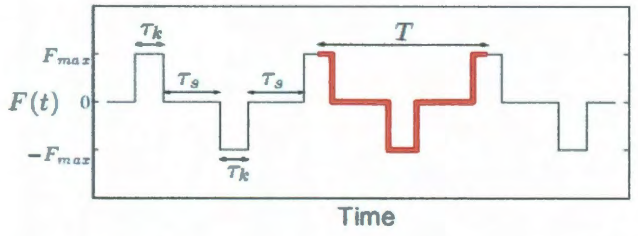

Figure 4.1 : The externally applied electric force. The duration of each kick is τ_k and the separation between consecutive kicks is τ_s. Hence, the total kicking period is $T = 2\tau_k + 2\tau_s$. The bold line denotes one cycle of the Poincaré map (the kicking period).

Our current experimental set up is capable of creating quasi-1D Rydberg states. In this case, the electron dynamics can be modeled as it going back and forth along a single one-dimensional radial half-line. In the one-dimensional limit, the electron orbit collapses onto a half-line, with the nucleus at $r = 0$, with the electron restricted to $r \geq 0$ where r is the electron distance from the nucleus. The electron Hamiltonian thus becomes

$$H(r, p_r, t) = \frac{p_r^2}{2} - \frac{1}{r} - rF(t), \tag{4.1}$$

where p_r is the electron momentum, F(t) is an external time-dependent electric force, and atomic units are used throughout. The sequence of the kicks examined in theoretical studies is shown on Fig. 4.1 and comprises alternating positive and negative square kicks (a sequence which we cannot reproduce exactly in our current apparatus). Positive F(t) corresponds to kicking the electron away from the nucleus and

[1] Much of the discussion in this section follows that of K. Burke [7].

negative F(t) corresponds to kicking toward the nucleus. τ_k is the kick duration, τ_s is the time separation between consecutive kicks, and $T = 2\tau_k + 2\tau_s$ is the total kicking period. F_{max} is the maximum amplitude of the force. With these parameters, we can define the integrated strength of each of the kicks, as

$$\Delta p = \tau_k F_{max}. \tag{4.2}$$

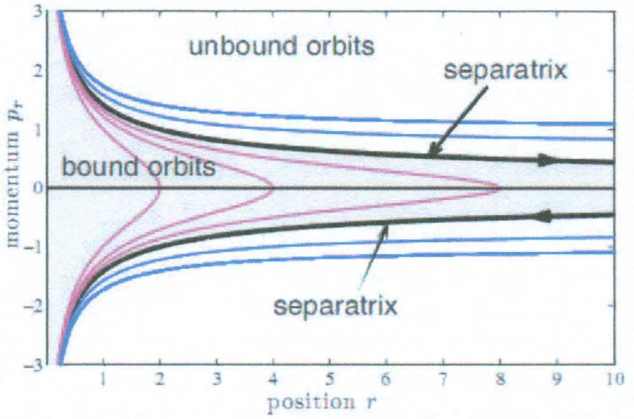

Figure 4.2 : Unkicked trajectories. The shaded region is the negative energy region where all the orbits are bounded. The separatrix (thick black line) separates the bound [thin magenta (light gray) lines] from the unbound [thin blue (dark gray) lines] orbits.

Fig. 4.2 shows the phase space of the unkicked $[F(t) = 0]$ classical one-dimensional hydrogen atom. In this case the system is Hamiltonian and independent of time, so the energy E is constant along an electron orbit. At $E = 0$, the turning point $(r, p_r) = (\infty, 0)$ is at infinity and the Kepler period is infinite. This zero-energy orbit forms a separatrix. And it acts as a barrier to transport between the bound and unbound orbits in phase space. To illustrate the specific motion of one electron, a discrete-

time Poincaré map $(r, p_r) \rightarrow (r', p_r')$ can be defined by stroboscopically recording (r, p_r) once per kicking period T instead of continuously tracking the classical electron orbit. A sequence of operations are applied to the system (r, p_r) by the electric pulses corresponding to the single "iterate" shown in red in Fig 4.1. First of all, the electron is subjected to "half" of the kick away from the nucleus. It then evolves freely for time τ_c, follow which a "full" kick is applied toward the nucleus. After this the electron evolves freely for another time τ_c whereupon another half-kick is applied away from the nucleus. The final position and momentum (r', p_r') are then probed.

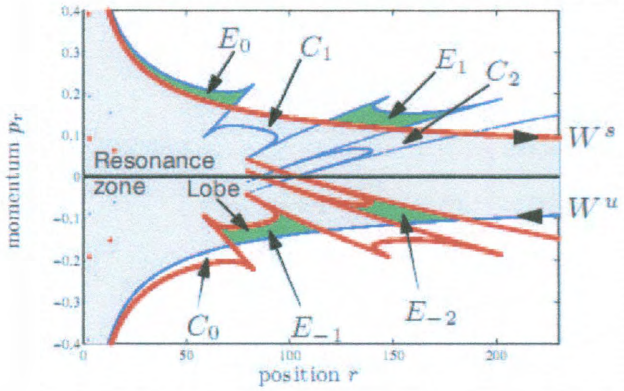

Figure 4.3 : A representative homoclinic tangle for the hydrogen atom exposed to alternating positive and negative kicks. The red line represents the stable manifold W^s and the blue line represents the unstable manifold W^u. The escape lobes E_k of the homoclinic tangle are shaded green and the resonance zone is shaded light gray.

For the unkicked case, the "turning point" of the separatrix is $(r, p_r) = (\infty, 0)$. Since the Coulomb force vanishes at $r = \infty$, this is a fixed point of the system. And the fixed point $(\infty, 0)$ is the point upon which the forward time evolution of every point on the separatrix converges. Thus, this implies that the separatrix (including both

the upper and lower branches) can be interpreted as the stable manifold of the fixed point $(\infty, 0)$. As mentioned as a definition in Chapter 2, a stable (unstable) manifold consists of all points whose forward (backward) time evolution converges upon a fixed point or other invariant set. Further more, the separatrix is also the unstable manifold of $(\infty, 0)$, since the backward iterates of every point on the separatrix also converge upon $(\infty, 0)$. Thus, the stable and unstable manifolds of $(\infty, 0)$ coincide with each other and with the separatrix for the unkicked case. As in the unkicked case, the map also has the same fixed point $(\infty, 0)$ to which stable manifold W^s and unstable manifold W^u are attached. However, in the kicked case, the structure of these manifolds is drastically different as shown on Fig. 4.3. The lower branch of the unstable manifold follows a curve whose shape closely resembles the separatrix in the unkicked case. Upon reflection off the nucleus, the upper branch of the unstable manifold continues along a complicated winding curve that repeatedly crosses the stable manifold W^s. Hence, the unstable manifold does not coincide with the stable manifold as it did in the unkicked case. Instead, the stable and unstable manifolds together form a complicated pattern of intersecting manifolds, called a homoclinic tangle, as mentioned on Chapter 2 [3, 12, 13] which defines the inner gray zone (roughly the "bound" electron states) and the outer white zone (the "ionized" states.) The tangle also defines regions called lobes, which fall into two categories, those that govern electron capture (C_n) and those that govern electron escape/ionization (E_n). E_n is the region of phase space bounded by the upper branches of W^u and W^s

between the nucleus and the closest W^s and W^u intersection with positive p_r. On the Poincaré map applying one period of kicking is called one mapping. And mapping the lobe E_0 forward and backward defines the escape lobes E_k, with $0 < k < \infty$ and $-\infty < k < 0$, respectively. Thus, lobe E_k maps to lobe E_{k+1}. In other words, when an electron trajectory maps from inside the resonance zone to outside the resonance zone, it is mapping from E_{-1} to E_0, which leads to escape, or ionization, of an electron trajectory. We call the E_k lobes, $-\infty < k < \infty$, escape lobes, since the lobe E_0 subsequently maps to E_1, then to E_2, E_3, and so forth, never to return to the resonance zone. Similarly, the capture lobe C_0 is the region of phase space bounded by the lower branches of W^u and W^s between the nucleus and the closest W^s and W^u intersection with negative p_r. And after one kicking period mapping the C_0 into the C_1 lobe corresponds to the electron trajectories mapping from the outside to the inside the resonance zone, which implies capture. Under the forcing dynamics, $E_n \mapsto E_{n+1}$ and $C_n \mapsto C_{n+1}$. The critical step for ionization is the $E_{-1} \mapsto E_0$ transition as this promotes electron states from bound to ionized. Thus, to study the ionization, the escape lobe is the key. We use the turnstile related concept to conclude transport into and out of the resonance zone. The occurrence of ionization indicates that the E_{-1} lobe (inside the resonance zone) maps into the E_0 lobe (outside the resonance zone); and capture happens when the C_0 lobe (outside the resonance zone) maps into the C_1 lobe (inside the resonance zone).

The major concern of the theoretical work lies in the influence of kicking param-

eters on lobe geometry. It has been analytically determined how the kicking period and kicking strength influence the lobe length, width and area [7],

$$lobe\ width \propto T, \tag{4.3}$$

$$lobe\ length \propto \Delta p/T^{1/3}, \tag{4.4}$$

and

$$lobe\ area \approx 1.404 \Delta p T^{2/3}. \tag{4.5}$$

Note that we restrict our attention to small kick strengths $\Delta p \ll 1$ and short kick durations $\tau_k \ll T$.

One of the effects we tested in the experiment is the variation in ionization probability with kick strength. Holding the kick duration τ_k and the kicking period T constant (Fig. 4.4) while changing the kick strength Δp the positions of the intersections between the stable and unstable manifolds do not move in phase space, and hence the width of the lobes remains constant with changing Δp. As shown on Fig. 4.4 a linear decrease in the area of the lobe resulting from the splitting between the stable and unstable manifolds decreases the area of the lobe, which verifies Eq. 4.4 and Eq. 4.5.

The other effect is the variation in ionization probability with the kicking period. We can see the behavior of the homoclinic tangle for increasing values of T when we keep τ_k and Δp constant and change the kicking period T by varying the separation time τ_s between consecutive positive and negative kicks. We can identify the intersection between the stable and unstable manifolds to the left of the E_1 lobe by the

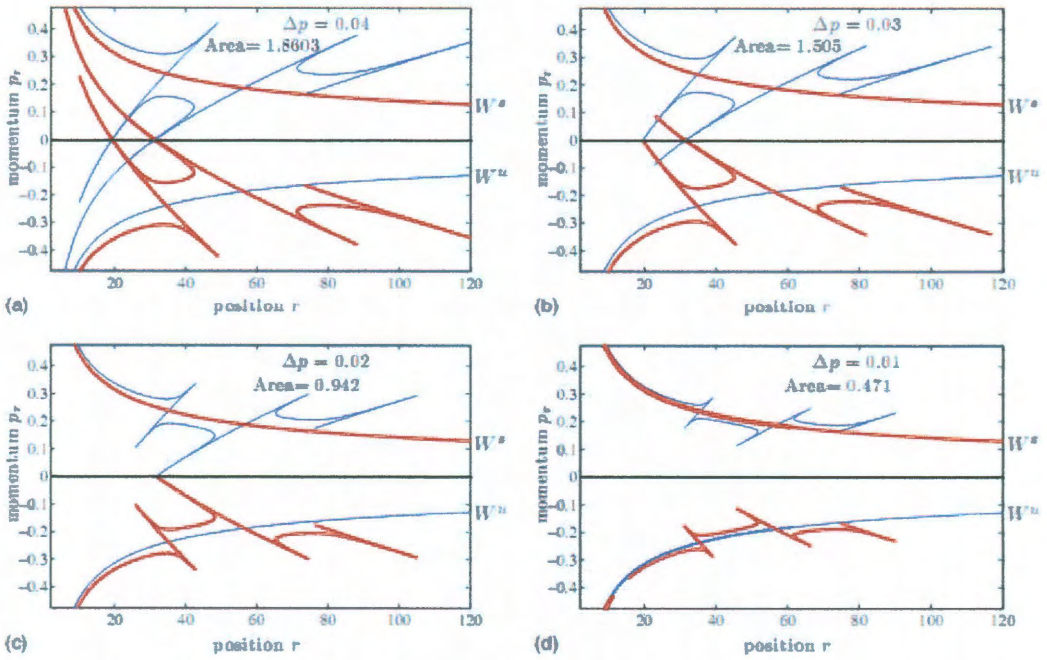

Figure 4.4 : The influence of changing the kick strength Δp on the size of the lobes in the homoclinic tangle. The kick strength decreases in magnitude from $\Delta p = 0.04$ in figure (a) to $\Delta p = 0.01$ in figure (d). The length of the kick $\tau_k = 1$ and the kicking period $T = 202$ are kept constant in all four figures.

black dots in each figure. As T increases the marked intersection (and in fact all intersections) moves away from the nucleus, and furthermore, the lobe widths increase. This is confirmed by the equation [7]

$$(r, p_r) = \left(\frac{(3T)^{2/3}}{2}, \pm \frac{2}{(3T)^{1/3}} \right), \tag{4.6}$$

where r is the radial coordinate and p_r is the momentum.

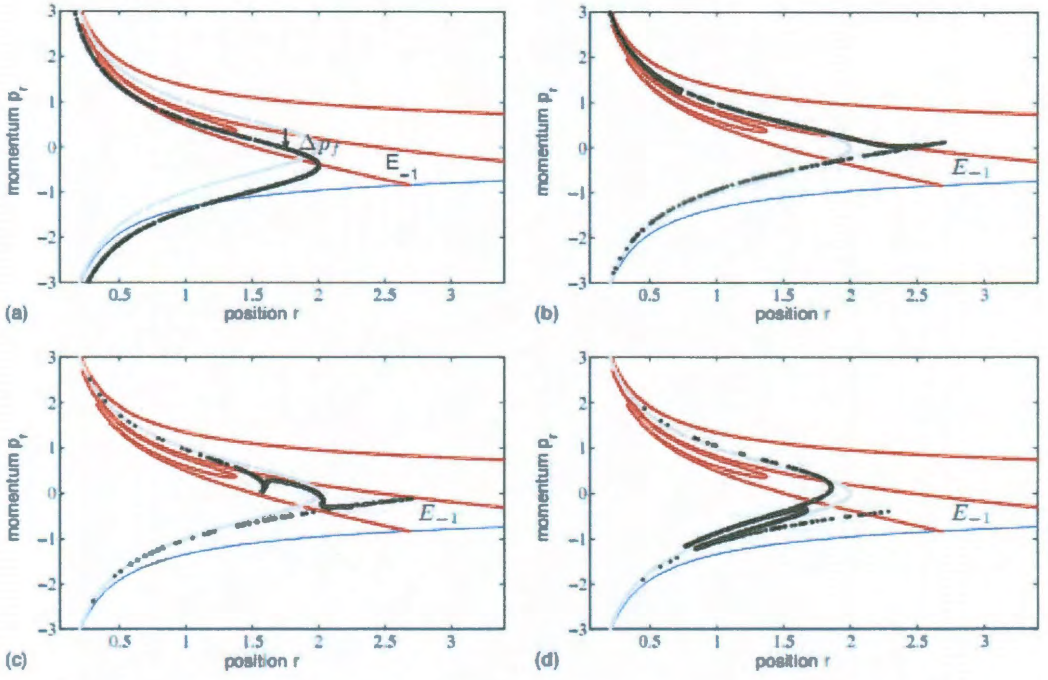

Figure 4.5 : Figure (a) shows the initial ensemble on the energy shell $E = -1/2$ in light gray and the shifted ensemble immediately after the negative kick Δp_f in black. (The actual Δp_f is five times smaller than shown; we have magnified it here to show the shift more clearly.) Figures (b)-(d) show the new ensemble focused just above ($\tilde{\tau}_f = 4.7ns$), inside ($\tilde{\tau}_f = 6.1ns$), and just below ($\tilde{\tau}_f = 8.1ns$) the E_{-1} lobe.

4.2 Experiment I: Dependence of ionization on the position of the electronic state relative to the escape lobe

The first experiment consists of exposing an energy shell ($n = 306$ and also $n = 350$) to a small focusing kick, letting the resulting ensemble evolve for some time until it is localized in phase space and finally exposing it to one period of alternating kicks as shown in the previous section (half of the positive kick; time evolution; full negative kick; time evolution; half of the positive kick). As demonstrated previously [7], the

small focusing kick Δp_f slows down all the electrons with positive momenta and speeds up those with negative momenta. This perturbation, in essence, allows those electrons that sped up to "catch up" to those electrons that slowed down, resulting in a partial focusing in phase space. The pulses used in the present work are not perfect "square waves" having finite rise and fall times. Furthermore, because we are more concerned about the size of the kick Δp_f, rather than the width of a pulse, instead of halving the width of the positive kick we halve its amplitude, for practical convenience. The aim of the present work is to demonstrate that the phenomena observed in the behavior of the survival probability and ionization fraction cannot be understood only as a resonance with the classical Kepler period or the kicking period but rather must invoke the notion of a turnstile. Varying the focusing time allows the focused state to be selectively placed mostly just above, inside, or just below the E_{-1} lobe by adjusting $\tilde{\tau}_f$ to 4.7 ns, 6.1 ns, and 8.1 ns, respectively, as shown in Fig. 4.5(b) – 4.5(d).

Fig. 4.6 shows the experimental results obtained using $n \sim 306$ Rydberg atoms. A periodic drop is seen in the survival probability which coincides with the classical period of the $n = 306$ energy shell. The ionization process is governed by the turnstile. Picking the particular values of the kick strength, kick duration and kicking period automatically fixes both the size and the shape of the turnstile, and its position in phase space. At t=0 the initial ensemble is located inside the escape lobe of the turnstile, which leads to the occurrence of the first dip in the survival probability.

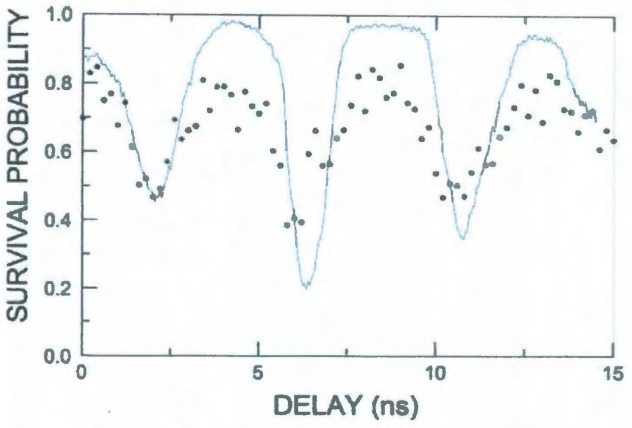

Figure 4.6 : Experimental results for survival probability as a function of delay time between the localizing kick and the start of the HCP sequence for $n \sim 306$ atoms. The solid lines show the prediction of 1D theory.

Since the initial focusing kick is very small, the energy distribution of the ensemble is also small, and all the electrons have roughly the same classical Kepler period. Hence, there is a dip in the survival probability about every 4ns. The position of the first dip is governed by the turnstile, and changing the kicking parameters would change its position. Because the position of the ionization lobe moves closer to the nucleus as the kicking period decreases, decreasing the kicking period should move the first dip out to longer delay times. Fig. 4.7 and Fig. 4.8 show experimental results for different values of T and $n = 306$ and $n = 350$. In each case periodic oscillations at the corresponding Kepler frequencies are seen, the phase of these oscillations depending markedly on T. A comparison between the predicted 1D and observed phases for $n = 350$ are presented in Fig 4.9. As expected, the sine wave maxima and minima move to shorter delay times as the kicking period increases.

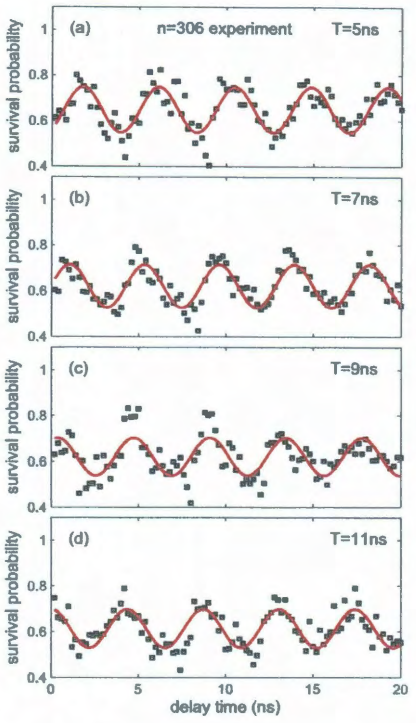

Figure 4.7 : n=306 experimental data for the periods T indicated. The solid line shows a sine wave fit to the data.

4.3 Experiment II: Dependence of ionization on lobe length

To measure how increasing Δp increases the splitting between the stable and unstable manifolds we expose highly excited ($n = 306$) quasi-1D states to one kicking period and measure the fraction f of the electron trajectories that ionize. Since the ionization corresponds to mapping from the E_{-1} lobe to the E_0 lobe, the ones that start within the E_{-1} lobe are the only trajectories that ionize after one kicking period.

Numerical 1D results are shown in Fig. 4.10. For $\Delta p = 0.1$ there is no overlap between the E_{-1} lobe and the starting distribution. Hence, no trajectories are ionized

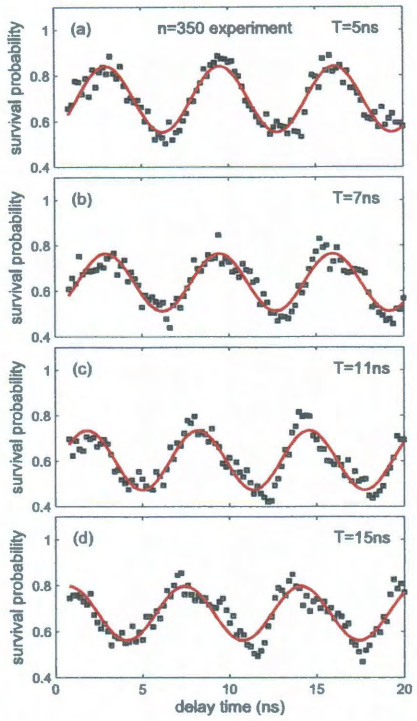

Figure 4.8 : n=350 experimental data for the periods T indicated. The solid line shows a sine wave fit to the data.

after one kicking period. We can have the E_{-1} lobe intersects the starting distribution by increasing Δp to 0.5 increases the splitting between the stable and unstable manifolds. Further increases in Δp to 0.7 does not drastically change the overlap between the E_{-1} lobe and the starting distribution.

Besides the kick strength, the kick period is also a parameter that influences the ionization fraction. Fig. 4.11 shows the behavior of the ionization fraction as a function of kick strength for kicking periods ranging from 2ns to 13ns. For small values of the kicking period, the ionized fraction resembles a step-function, with an

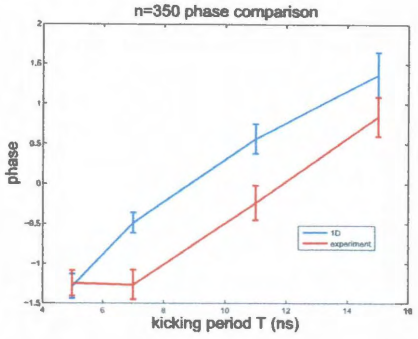

Figure 4.9 : Phase comparison between experimental data and 1D simulations for n=350 and T = 5 to 15 ns.

initial rapid rise, followed by a sharp transition (at the "shoulder") into a much more gradually rising plateau. For larger values of the kicking period, the sharp transition at the shoulder becomes more subtle, and eventually disappears entirely around T $\sim$ 10ns. Above this kicking period, the plot is more "s" shaped. The sharp rise can also be seen in the experimental results. Figs. 4.12, 4.13, 4.14, 4.15, 4.16 show a comparison of the experimental results with the numerical 1D results. They agree with each other well. For small values of the kick strength, the ionization fraction is zero as the escape lobe does not overlap with the initial distribution. Since the length of the lobe is proportional to the kick strength according to Eq. 4.4, the tips of the horns begin to overlap with the energy shell as Δp increases. This triggers a rapid rise in the ionization fraction which culminates with the shoulder. The shoulder occurs when the middle part of the lobe finally overlaps with the energy shell. The lobes are narrower at the horn end, so further increase in the kick strength lead to a slow increase in the ionization fraction after the shoulder. Furthermore, Eq.4.3 shows

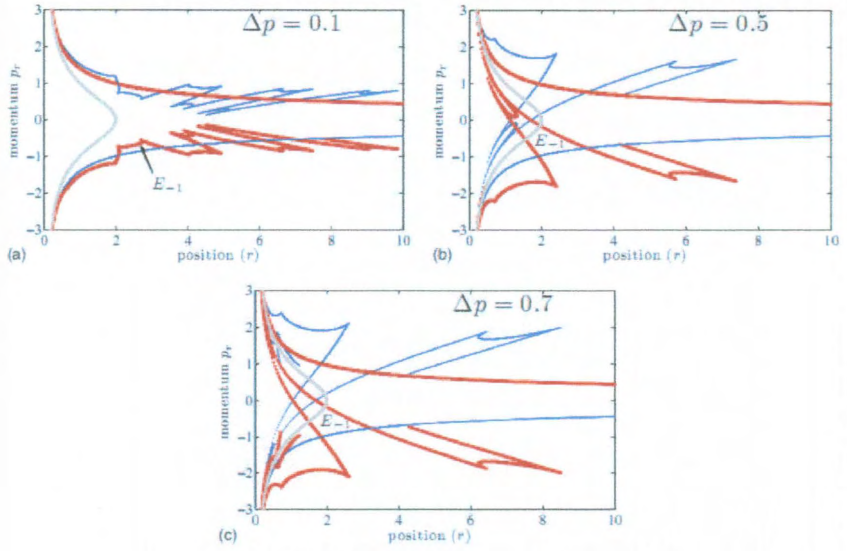

Figure 4.10 : Effect of the kick strength Δp. For all three figures $\tilde{\tau}_k = 500ps$ and $\tilde{T} = 3ns$. The gray curve represents the invariant classical distribution on the energy shell $E = -1/2$. For clarity, only the escape lobe E_{-1} is labeled.

that linearly increasing the kicking period linearly increases the width of the lobe. In other words, the wider the lobe is, the greater the overlap with the energy shell will be, and the greater the ionization fraction will be as well. As mentioned in Ref. [7], the critical value of the kick strength for which the shoulder appears depends on T, so the increase in the kicking period moves the position of the shoulder to larger values of the kick strength. When the kicking period reaches a critical value of roughly twice the Kepler period of the energy shell, the shoulder disappears.

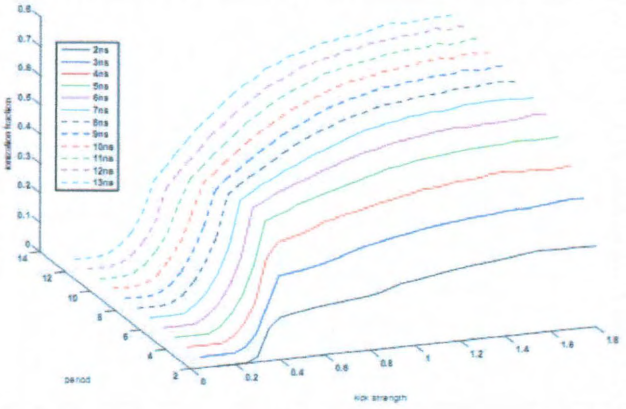

Figure 4.11 : Numerical 1D results. Calculated ionization fraction as a function of the kicking strength for $n = 306$ and for the time periods T indicated

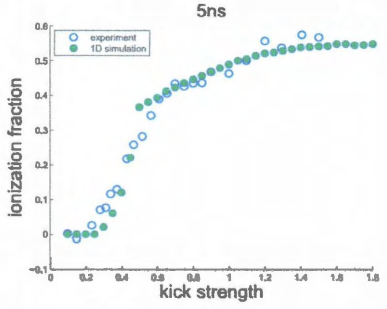

Figure 4.12 : Comparison between experimental and numerical 1D results for $n = 306$ and T=5ns.

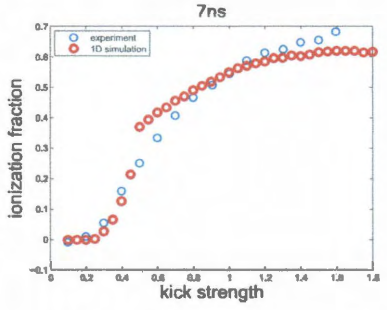

Figure 4.13 : Comparison between experimental and numerical 1D results for $n = 306$ and T=7ns.

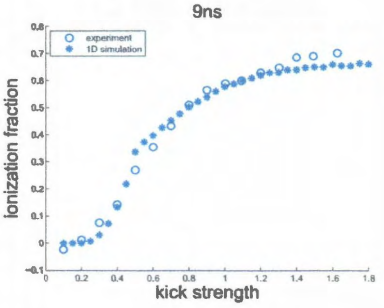

Figure 4.14 : Comparison between experimental and numerical 1D results for n = 306 and T=9ns.

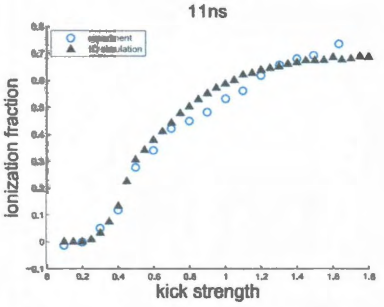

Figure 4.15 : Comparison between experimental and numerical 1D results for n = 306 and T=11ns.

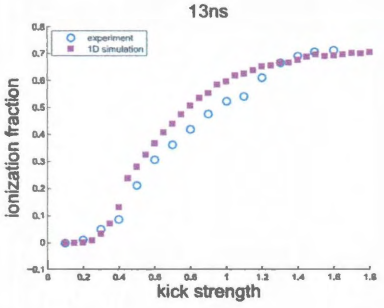

Figure 4.16 : Comparison between experimental and numerical 1D results for n = 306 and T=13ns.

Chapter 5

Conclusions and Outlook

The present work demonstrates the influence of tangles on the ionization process. The first experiment illustrates the sensitivity of placing the initial electronic state inside or just outside the turnstile lobe. For example, even though two states may be only slightly different and have the same energy distribution and be subjected to the same sequence of kicks, the times scales of their ionization can be notably different, depending on whether the initial state resides inside or outside the lobe. Thus measurements of survival probability provide a laboratory to probe the position of the lobes in phase space. The second experiment shows that the ionization fraction after one kicking period undergoes a steplike increase as a function of the kick strength.

This work focuses on how the ionization of highly excited Rydberg atoms is governed by a homoclinic tangle and associated phase-space turnstile when the atoms are exposed to alternating positive and negative kicks. The aim of the experiments is to develop an understanding of how the ionization process depends on experimental parameters which, in this case, are kick duration, kick strength, and total kicking period.

This work demonstrates that turnstiles can not only elucidate fundamental ionization mechanisms, but also provide a convenient laboratory for studying chaotic

transport and escape furnishing new insights into both atomic physics and nonlinear dynamics.

Bibliography

[1] C. Beenakker, *Rev. Mod. Phys.* **69**, 731 (1997).

[2] T. Pohl, T. Pattard, and J. M. Rost, *Phys. Rev. A* **68**, 010703 (2003).

[3] R. S. MacKay, J. D. Meiss, and I. C. Percival, *Physica D* **13**, 55 (1984).

[4] S. Wiggins, *Chaotic Transport in Dynamical Systems* (Springer-Verlag, New York, 1992).

[5] H. Friedrich, *Theoretical Atomic Physics* (Springer-Verlag, Berlin Heidelberg, 1990).

[6] F. B. Dunning, J. J. Mestayer, C. O. Reinhold, S. Yoshida, and J. Burgdörfer, *J. Phys. B* **42**, 022001 (2009).

[7] K. Burke, and K. A. Mitchell, *Phys. Rev. A* **80**, 033416 (2009).

[8] S. R. Channon, J. L. Lebowitz, *Ann. New. York Acad. Sci.* **357**, 295 (1980).

[9] J. H. Bartlett, *Celest. Mech.* **28**, 295 (1982).

[10] O. Teschke, J. R. Whinnery, and A. Dienes, *IEEE J. Quantum Electron.* **QE-12**, 513 (1976).

[11] T. F. Johnston, Jr., R. H. Brady, and W. Proffitt, *Applied Optics* **21**, 2307 (1982).

[12] K. A. Mitchell, J. P. Handley, B. Tighe, A. Flower, and J. B. Delos, *Chaos* **13**, 880 (2003).

[13] P. Collins, *Dyn. Syst* **19**, 1 (2004) .

[14] A. Messiah, *Quantun Mechanics* (North-Holland, 1970).

[15] C. L. Stokely, J. C. Lancaster, F. B. Dunning, D. G. Arbó, C. O. Reinhold, and J. Burgdörfer, *Phys. Rev. A* **67**, 013403 (2003).

[16] T. P. Hezel, C. E. Burkhardt, M. Ciocca, and J. J. Leventhal, *Am. J. Phys.*, **60**, 324 (1992).

[17] J. J. Mestayer, B. Wyker, J. C. Lancaster, F. B. Dunning, C. O. Reinhold, S. Yoshida, and J. Burgdörfer, "Realization of localized Bohr-like wavepackets", (submitted, 2008).

[18] M. T. Frey, F. B. Dunning, C. O. Reinhold, and J. Burgdörfer, *Phys. Rev. A.* **53**, R2929 (1996).

[19] M. T. Frey, Ph.D. Thesis, Physics & Astronomy, Rice University, (1996).

[20] H. Goldstein, C. Poole, and J. Safko, *Classical Mechanics*, 3rd ed., (Addison Wesley, New York, 2002).

[21] T. F. Gallagher, *Rydberg Atoms* (Cambridge University Press, New York, 1992).

[22] W. Zhao, J. C. Lancaster, F. B. Dunning, C. O. Reinhold, and J. Burgdörfer, *Phys. Rev. A*, **69**, 41401 (2004).

[23] M. T. Frey, X. Ling, B. G. Lindsay, K. A. Smith, and F. B. Dunning, *Rev. Sci. Instrum.* **64**, 3649 (1993).

[24] W. Zhao, Ph.D. Thesis, Physics & Astronomy, Rice University, (2007).

[25] B. Wyker, M.S. Thesis, Physics & Astronomy, Rice University, (2008).

[26] B. G. Zollars, *CR-699-21 Single Frequency Ring Laser Alignment Manual*, (Internal Dunning Lab Documentation, Houston, TX, 1985).

[27] *Coherent CR-699 Ring Laser Manual*, (Coherent, Palo Alto, CA, 1982).

[28] B. G. Lindsay, *Superlock Manual*, (Internal Dunning Lab Documentation, Houston, TX, 1991).

[29] J. L. Hall and S. A. Lee, *Appl. Phys. Lett* **29**, 367 (1976).

[30] *Wavetrain Tunable CW Frequency Doubler User Manual*, Version 3.2, (Spectra-Physics GmbH, Berlin, 1999).

[31] R. W. Drever, J. L. Hall, et al., *Appl. Phys. B* **31**, 97 (1983).

[32] *KBL 25RS Product Documentation*, (Sjuts Optotechnik GmbH, Göttingen).

[33] B. E. Tannian, C. L. Stokely, F. B. Dunning, C. O. Reinhold, and J. Burgdörfer, *Phys. Rev. A*, **64**, 021404 (2001).